



RESEARCH ARTICLE

10.1002/2014GC005464

Key Points:

- New $^4\text{He}/^3\text{He}$ data are presented from the Appalachian Mountains
- We present a 3-D He production-diffusion model for a single crystal
- We resolve intracrystal variations in diffusivity due to radiation damage

Correspondence to:

M. Fox,
matthew.fox@berkeley.edu

Citation:

Fox, M., R. E. McKeon, and D. L. Shuster (2014), Incorporating 3-D parent nuclide zonation for apatite $^4\text{He}/^3\text{He}$ thermochronometry: An example from the Appalachian Mountains, *Geochem. Geophys. Geosyst.*, 15, 4217–4229, doi:10.1002/2014GC005464.

Received 18 JUN 2014

Accepted 14 OCT 2014

Accepted article online 20 OCT 2014

Published online 10 NOV 2014

Incorporating 3-D parent nuclide zonation for apatite $^4\text{He}/^3\text{He}$ thermochronometry: An example from the Appalachian Mountains

Matthew Fox^{1,2}, Ryan E. McKeon³, and David L. Shuster^{1,2}

¹Department of Earth and Planetary Science, University of California, Berkeley, California, USA, ²Berkeley Geochronology Center, Berkeley, California, USA, ³Division of Geological and Planetary Sciences, California Institute of Technology, Pasadena, California, USA

Abstract The ability to constrain km-scale exhumation with apatite $^4\text{He}/^3\text{He}$ thermochronometry is well established and the technique has been applied to a range of tectonic and geomorphic problems. However, multiple sources of uncertainty in specific crystal characteristics limit the applicability of the method, especially when geologic problems require identifying small perturbations in a cooling path. Here we present new $^4\text{He}/^3\text{He}$ thermochronometric data from the Appalachian Mountains, which indicate significant parent nuclide zonation in an apatite crystal. Using LA-ICPMS measurements of U and Th in the same crystal, we design a 3-D model of the crystal to explore the effects of intracrystal variability in radiation damage accumulation. We describe a numerical approach to solve the 3-D production-diffusion equation. Using our numerical model and a previously determined time temperature path for this part of the Appalachians, we find excellent agreement between predicted and observed $^4\text{He}/^3\text{He}$ spectra. Our results confirm this time-temperature path and highlight that for complex U and Th zonation patterns, 3-D numerical models are required to infer an accurate time-temperature history. In addition, our results provide independent and novel evidence for a radiation damage control on diffusivity. The ability to exploit intracrystal differences in ^4He diffusivity [i.e., temperature sensitivity] greatly increases the potential to infer complex thermal histories.

1. Introduction

Apatite (U-Th)/He thermochronometry has been used extensively to quantify timing of km-scale exhumation, due to its ability to constrain cooling down to temperatures as low as 30°C [Zeitler *et al.*, 1987; Farley, 2000; Shuster and Farley, 2004; Shuster *et al.*, 2006; Flowers *et al.*, 2009]. The system is based on the temperature-dependent diffusive loss of radiogenic ^4He atoms (i.e., produced by alpha decays along U and Th decay chains) between 30 and 80°C [Farley *et al.*, 1996]. To first order, the solution to the (U-Th)/He age equation can be interpreted as the time since a rock exhumed from depths of typically 1–3 km to the surface [Ehlers and Farley, 2003]. However, the thermal history constrained by a single (U-Th)/He “age” is non-unique and thus additional data are required to quantify either an exhumation rate or history. In addition, crystal-specific characteristics, such as U and Th zonation and bulk concentrations, influence the net rate of ^4He diffusion; in some scenarios, these characteristics are required to extract an accurate time-temperature history [Farley *et al.*, 2011; Gautheron and Tassan-Got, 2010; Flowers and Farley, 2012; Fox and Shuster, 2014].

Apatite $^4\text{He}/^3\text{He}$ thermochronometry constrains the spatial distribution of ^4He within a single apatite crystal, thus greatly reducing the number of permissible time-temperature paths a sample could have experienced [Shuster and Farley, 2004]. The spatial distribution can be inferred through stepwise degassing analysis of crystals containing a spatially uniform distribution of proton-induced ^3He [Shuster *et al.*, 2004]. However, this ^4He spatial distribution is not simply a function of temperature-dependent diffusion: it also depends on the ^4He ejection profile [Farley *et al.*, 1996; Shuster and Farley, 2004] and the spatial distribution of U and Th within the crystal [Farley *et al.*, 2011], which can be measured using laser ablation inductively coupled plasma mass spectrometry (LA-ICPMS) [Farley *et al.*, 2011].

Alpha decays along U- and Th-decay chains produce recoil-induced “radiation damage” within the apatite crystal lattice [Shuster *et al.*, 2006; Shuster and Farley, 2009]. At sufficiently low temperatures (< ~110°C), the

accumulation of such damage has been observed to cause crystal-scale He diffusivity in apatite to decrease over time at a given temperature [Shuster *et al.*, 2006]. Conversely, if a sample is then taken to high temperatures ($> \sim 50^{\circ}\text{C}$), previously accumulated damage will “anneal” back to a crystalline state, thus returning He diffusivity to higher values [Shuster and Farley, 2009]. By analyzing different apatite crystals spanning a range of U and Th concentrations (or effective uranium, $e\text{U} = [\text{U}] + 0.235[\text{Th}]$) and a range of thermal histories, models have been developed that account for variations in He retentivity as a function of both the accumulation and annealing of radiation damage [Shuster *et al.*, 2006; Flowers *et al.*, 2009; Gautheron *et al.*, 2009]. These models have been used to infer thermal histories by exploiting intercrystal age dispersion for crystals that experienced the same cooling history [Flowers, 2009; Ault *et al.*, 2009; Flowers and Kelley, 2011; McKeon *et al.*, 2014]. In addition, these data sets have also helped validate the radiation damage control of diffusion kinetics. However, ^4He implantation [Spiegel *et al.*, 2009] and the potential influence of broken crystals on calculated (U-Th)/He ages [R. W. Brown *et al.*, 2013] have been used to explain similar age dispersion in data sets and may obscure the control of radiation damage on He diffusivity.

Numerical experiments have explored the sensitivity of stepwise degassing $^4\text{He}/^3\text{He}$ data to anisotropic diffusion, broken crystals, and spatially variable ^4He production; the results highlight a need to account for these complexities in certain cases [Farley *et al.*, 2010]. In addition, the influence of radiation damage accumulation and annealing causes spatial variability in He diffusion kinetics, and when simplified using a spherical approximation, such variability can be treated numerically [Farley *et al.*, 2011; Flowers and Farley, 2012; Fox and Shuster, 2014]. This is accomplished by converting observed spatial distributions of U and Th (e.g., via LA-ICPMS analysis; Farley *et al.*, 2011) into a spherical model with an equivalent surface area to volume ratio as the analyzed crystal and expressing an effective eU concentration along the radius. However, if the zonation pattern is poorly represented with a spherical geometry, a potential limitation with this approach is that this spatial transformation results in averaging and smoothing of zonation patterns. In turn, the accuracy and suitability of this transformation is difficult to assess.

Here we describe a numerical model that solves the ^4He production diffusion equation in three dimensions. Our model accounts for spatial variability in U and Th, which leads to nonuniformity in both ^4He production and temperature-dependent He diffusivity. To demonstrate the utility of our numerical method, we interpret new $^4\text{He}/^3\text{He}$ data from the Appalachians where the time temperature history of the sample from which the crystal was derived, has been previously modeled using a complex data set from bulk apatite (U-Th)/He analysis [McKeon *et al.*, 2014]. The $^4\text{He}/^3\text{He}$ data are indicative of strong eU zonation, which is confirmed by U and Th mapping by LA-ICPMS from a polished section through the same crystal. The presence of strong eU zonation within the analyzed crystal is consistent with others from the same sample and others from the region as presented by McKeon *et al.* [2014]. We show that to yield internally consistent time-temperature paths that predict both the observed $^4\text{He}/^3\text{He}$ data of the crystal used here and the (U-Th)/He data set presented by McKeon *et al.* [2014] requires incorporating patterns of observed eU zonation in 3-D. Strong spatial variability in eU concentration has led to substantial structure in the intracrystal ^4He concentration, which provides independent evidence for a radiation damage control on diffusion kinetics.

2. Sample Location and Analytical Methods

2.1. Appalachian Mountains

The Appalachian Mountains of eastern North America were constructed through a series of collisional orogenies in the Paleozoic and then torn apart and rejuvenated during Mesozoic rifting that opened the Atlantic Ocean basin. Models predict that mountain ranges should decay when the tectonic-driving forces that built them cease [e.g., Tucker and Slingerland, 1994], which makes the persistence of high topography in the Appalachians difficult to explain in the context of an old and decaying mountain range [e.g., Pazzaglia and Brandon, 1996]. Long-term erosion rates inferred from low-temperature thermochronometry are low, at approximately 20 m/Ma [Blackmer *et al.*, 1994; Boettcher and Milliken, 1994; Miller and Duddy, 1989; Naeser *et al.*, 2004; Roden and Miller, 1989; McKeon *et al.*, 2014]. In addition, these rates are consistent with estimates of erosion rate averaged over the past 10,000s years derived from cosmogenic nuclide analysis [Pavich *et al.*, 1985; Matmon *et al.*, 2003; Hancock and Kirwan, 2007; Portenga *et al.*, 2013]. These low rates are inferred across a wide range of localities and seem at odds with unsteady sediment deposition rates in margin shelf-slope basins [Pazzaglia and Brandon, 1996], and localized evidence for considerable, recent river incision, drainage rearrangement,

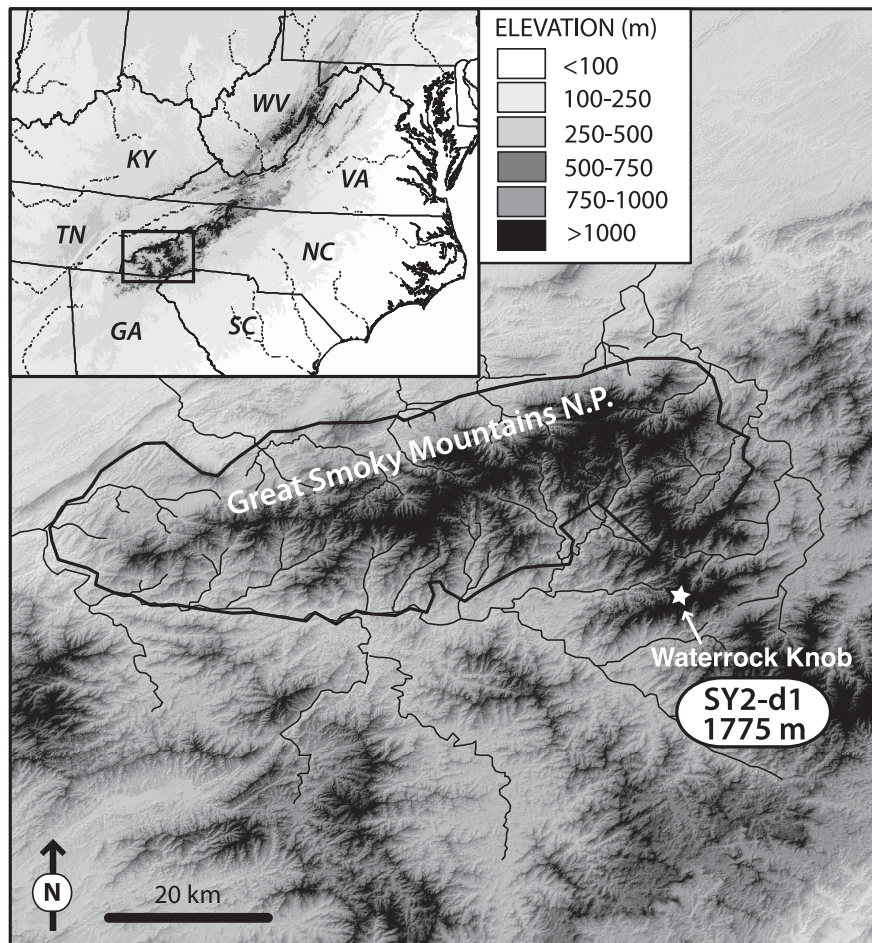


Figure 1. Map showing a digital elevation model of Waterrock Knob along the Blue Ridge Parkway where sample SY2-d1 was collected. Inset map shows the location of Waterrock Knob in eastern North America with abbreviated state names (GA: Georgia, KY: Kentucky, NC: North Carolina, SC: South Carolina, TN: Tennessee, VA: Virginia, WV: West Virginia) relative to the higher topography of the southern Appalachian Mountains.

and capture [Ward *et al.*, 2005; Prince *et al.*, 2011; Prince and Spotila, 2013; Gallen *et al.*, 2013], possibly driven by density anomalies in the mantle [Miller *et al.*, 2013; Moucha *et al.*, 2008].

2.2. $^4\text{He}/^3\text{He}$ Thermochronometry

The apatite crystal used for this study was derived from sample SY-2 of Mckeon *et al.* [2014] and is from the summit of Waterrock Knob, the highest point of the Blue Ridge Parkway in western North Carolina (Figure 1). Using an inverse approach, Mckeon *et al.* [2014] determined the thermal history of this sample using the bulk (U-Th)/He age-[eU] relationship of 12 single-crystal aliquots from SY-2, which suggests that the sample experienced steady cooling over the last 180 Myr at rates of $\sim 0.4^\circ\text{C}/\text{Myr}$. In order to independently test this inferred history and constrain cooling through lower temperatures, we collected new $^4\text{He}/^3\text{He}$ thermochronometric data from sample SY-2. Milligram quantities of apatite crystals separated from the sample of quartzo-feldspathic gneiss were irradiated with $\sim 1.0 \times 10^{16}$ p/cm² with incident energy of ~ 220 MeV over ~ 5 h at the Francis H. Burr Proton Therapy Center at the Massachusetts General Hospital [Shuster *et al.*, 2004]. Following irradiation, a single apatite crystal was selected (Figure 2a) based on the following selection criteria: (1) euhedral crystal with shortest axis greater than 60 μm ; (2) free of inclusions and fractures when observed with an optical microscope. This crystal was placed into a Pt-Ir packet and sequentially degassed at controlled temperatures using a pyrometer-controlled 70 W diode laser in the Noble Gas Thermochronometry Laboratory of Berkeley Geochronology Center following methods described in Shuster *et al.*, [2011]. Due to the relatively high concentration of radiogenic ^4He in the crystal ($\sim 10^{-9}$ mol/g),

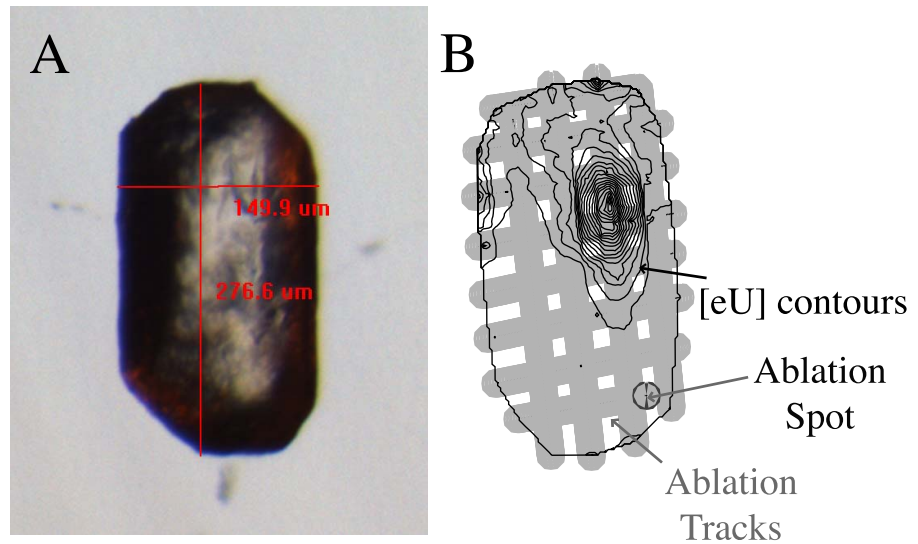


Figure 2. (a) Photomicrograph of sample SY2-d1 with grain dimensions indicated ($149.9 \times 276.6 \mu\text{m}$). (b) Map of grain surface showing the location and size of ablation tracks (gray lines) that were used for the collection of [eU] data. The [eU] contours (thin black lines) correspond to the different colors used to denote [eU] in Figure 3a. Of note is that the vast majority of the grain surface was sampled for [eU] analysis and that the zone of high [eU] is traversed completely by one track and cross cut by three others, making it unlikely that the high [eU] zone is the result of a micro inclusion not visible by optical grain selection.

$^4\text{He}/^3\text{He}$ ratios were measured with high precision (Table 1). The $^4\text{He}/^3\text{He}$ ratios increase systematically from initially low values and produce a release spectrum (Figure 4a) that is clearly inconsistent with a uniform spatial distribution of U and Th within the crystal. Since the $^4\text{He}/^3\text{He}$ data do not conform to the characteristic convex up pattern, they indicate particularly strong zonation in [eU].

2.3. LA-ICPMS Analyses of U and Th

To quantify the spatial distribution of U and Th within this apatite crystal, we followed the methods described by Farley *et al.* [2011] using the same LA-ICPMS system at Caltech and identical data reduction methods. We recovered the apatite crystal following $^4\text{He}/^3\text{He}$ analysis, mounted it in epoxy, and exposed an internal plane perpendicular to the shortest axis of the crystal at roughly half the depth through polishing.

Table 1. Apatite $4\text{He}/3\text{He}$ Stepwise Degassing Analysis of SY2-d1^a

Step	T (°C)	(+/-)	t (h)	[³ He]($\times 10^6$ atoms)	(+/-)1 σ	⁴ He/ ³ He	(+/-) 1 σ
1	180	3	1	0.059	0.005	0	127
2	225	3	0.5	0.857	0.029	34	9
3	260	1	0.38	1.377	0.037	88	7
4	300	1	0.51	2.761	0.053	131	4
5	300	2	0.66	1.559	0.039	166	7
6	310	2	0.66	2.029	0.045	223	7
7	330	2	0.46	1.772	0.042	234	7
8	340	2	0.45	1.645	0.041	262	8
9	350	2	0.48	1.712	0.041	295	9
10	350	5	0.66	1.525	0.039	331	10
11	370	0	0.53	1.278	0.035	402	13
12	400	6	0.48	1.687	0.041	444	12
13	410	1	0.5	1.596	0.04	533	14
14	420	1	0.56	1.462	0.038	676	18
15	440	1	0.63	1.538	0.039	807	20
16	475	4	0.5	1.285	0.036	943	26
17	500	3	0.5	0.811	0.028	995	36
18	600	3	0.5	0.928	0.03	783	26
19	700	10	0.5	0.185	0.012	451	53
20	900	2	0.5	0.001	0	5706	36134
21	900	5	0.5	b.d. ^b		b.d.	

^aMeasurement precision includes uncertainty in blank corrections.

^bb.d. is below detection limit.

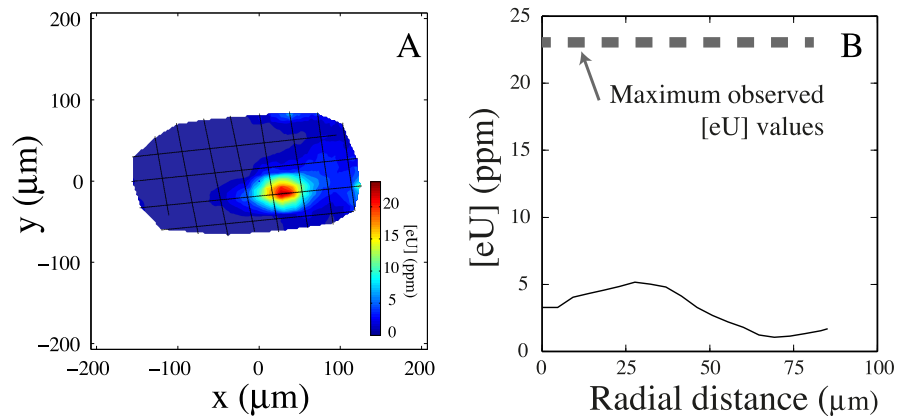


Figure 3. LA-ICPMS data collected for a single crystal from sample SYD-2 from the Appalachian Mountains. (a) Concentration of eU across a section of the same crystal measured by LA-ICPMS perpendicular to the shortest axis. (b) Spherical model of [eU] calculated from data shown in Figure 3a projected along a radial coordinate.

Laser ablation tracks (shown in Figure 2b) using a 20 μm diameter circular ablation spot began and ended in epoxy fully traversing the crystal and the crystal boundary was defined by tracking the rise of ^{44}Ca . Sensitivity for ^{238}U and ^{232}Th was calibrated using a similar track across Durango apatite (included in the grain mount) analyzed immediately prior to the analysis of SYD-d1. The resulting spatially referenced grid of ^{238}U and ^{232}Th measurements was converted to a 2-D color contour map of eU concentration using an inverse-distance-weighted algorithm [Shepard, 1968] in MATLAB with a radial distance limit of 20 μm and a power parameter of 0.7. The resulting map of eU values is shown in Figure 3a and highlights an enriched core with concentrations as high as 23 ppm, surrounded by eU concentrations between 2 and 5 ppm. We are confident that this enriched zone is not an inclusion because it is relatively large ($>50 \mu\text{m}$) and would have been identified at the time of crystal selection using the optical microscope. In addition, the variability in eU concentration is similar to that observed in other crystals from the same location [McKeon *et al.*, 2014] and also in other published apatite data sets from different locations [Farley *et al.*, 2011; Ault and Flowers, 2012; Flowers and Farley, 2012]. This 2-D eU map was then converted to a 1-D radial model of eU zonation as input for spherically symmetric models of ^4He production and diffusion as shown in Figure 3b. The mathematical framework for this conversion is described at length in Farley *et al.* [2011].

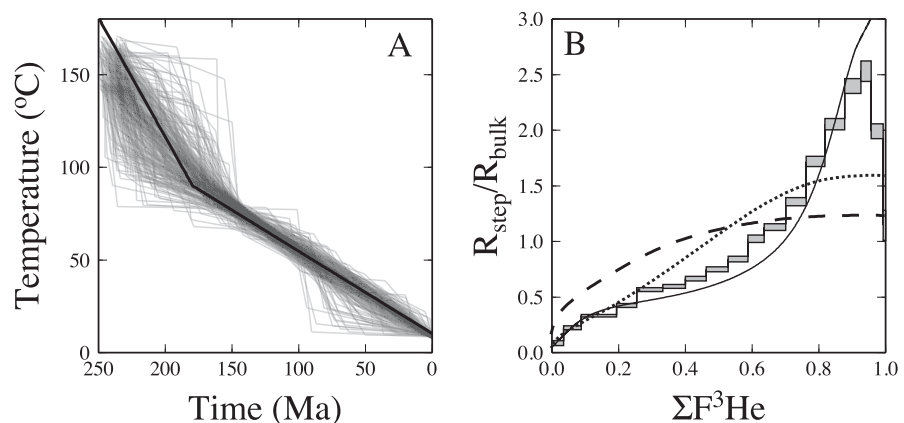


Figure 4. (a) Time-temperature path inferred for the sample SYD-2 determined from the analysis of (U-Th)/He age dispersion between a large population of apatites from this sample after McKeon *et al.* [2014]. The gray lines highlight paths that predicted the data well and the solid line is the representative cooling history used here. (b) Ratio evolution diagram showing the observed $^4\text{He}/^3\text{He}$ ratios (R_{step}), normalized to the bulk $^4\text{He}/^3\text{He}$ ratio (R_{bulk}), as a function of cumulative release fraction of ^3He ($\Sigma F^3\text{He}$). Model-predicted $^4\text{He}/^3\text{He}$ data assuming: (1) a spherical model with a uniform [eU] distribution, dashed line (model predicted age = 67.6 Ma); (2) a spherical model with radial symmetric zoning with [eU] values inferred from the LA-ICPMS data using the data reduction method of [Farley *et al.*, 2011], dotted line (model predicted age = 77.7 Ma); (3) 3-D geometry with estimated U and Th distributions using the method described in Section 4, solid black line (model predicted age = 63.4 Ma).

2.4. Failure of Simple Models of U and Th Zonation

To investigate the effects of U and Th zonation on the $^4\text{He}/^3\text{He}$ data of sample SY2-d1, we use the inferred cooling history for this crystal (Figure 4) after *McKeon et al.*, [2014]. Using this cooling history and assuming a spatially uniform distribution of eU and a spherical crystal geometry (following the numerical approach of *Ketcham* [2005]), we predict the $^4\text{He}/^3\text{He}$ data shown in Figure 2b. As expected, the modeled $^4\text{He}/^3\text{He}$ spectrum fails to predict the observed release spectrum. If we incorporate the eU map for this crystal observed via LA-ICPMS (Figure 3a) by spatial transformation to a radially symmetric description of eU zonation using the method of *Farley et al.* [2011], we begin to capture some of the structure in the $^4\text{He}/^3\text{He}$ spectrum. However, much structure in the data are not reproduced by this simplified model, which likely results from the spatial averaging introduced by translating the 2-D map into a 1-D radially symmetric model of [eU] distribution.

3. A 3-D Model of Production and Diffusion of ^4He

The fraction of He released during a specific degassing step is a function of three variables: (1) the spatial distribution of ^4He which is a function of the sample's geologic thermal history and also the distribution of [U] and [Th]; (2) the spatial distribution of diffusivity, which is also a function of the thermal history and the distribution of [U] and [Th]; and (3) the crystal geometry. Therefore, below we describe a numerical model designed to account for these factors.

The evolution of age τ , (i.e., ^4He concentration divided by the production rate) through time can be described with using the 3-D production diffusion equation:

$$\frac{\partial \tau}{\partial t} = D \nabla^2 \tau + P \quad (1)$$

where D is the diffusivity and P is the production rate of ^4He , both of which may vary as a function of space and time. D can be defined based on the previous thermal history using a radiation damage and annealing model [*Flowers et al.*, 2009]. P is a function of the spatial distribution of [U] and [Th] combined with the redistribution of alpha particles due to the effects of long-stopping distances. In addition, we assume that the concentration of ^4He outside of the crystal is equal to zero at all time. When we simulate a step degassing experiment, P is set equal to 0.

Both analytical and numerical methods have been used to solve the production-diffusion equation in order to interpret (U-Th)/He ages. Analytical solutions for the production and diffusion of noble gases in solids exist for simple geometries [e.g., sphere, cylinder, plane slab, cube; *Fechtig and Kalbitzer*, 1966; *McDougall and Harrison*, 1988; *Wolf et al.*, 1998; *Watson et al.*, 2010]. However, numerical models are generally required to account for changes in temperature-dependent diffusivity through time. Numerical methods have been developed for simple spheres, finite cylinders, and rectangular blocks that incorporate the effects of spatially nonuniform ^4He production using the eigenmode method [*Meesters and Dunai*, 2002a, 2002b] and also for arbitrary crystal geometries using a finite difference method [*Herman et al.*, 2007]. More recently, *Gautheron and Tassan-Got* [2010] used a Monte Carlo simulation to investigate the effects of isotropic and anisotropic diffusion for realistic crystal geometries, and *Huber et al.* [2011] adopted a lattice Boltzmann approach to model diffusion from complex 3-D geometries having isotropic, temperature-independent anisotropic, and temperature-dependent anisotropic diffusivity. However, none of these approaches have explored the effects of spatial and temporal variations in diffusivity on $^4\text{He}/^3\text{He}$ release spectra.

3.1. Spatial Discretization

We discretize 3-D space into nodes with a typical spacing of $10 \times 10 \times 10 \mu\text{m}$ and define the crystal within this domain. As discussed below, the numerical method used for the temporal integration requires that the number of nodes across each dimension be $2^n + 1$, where n is an integer. Increasing n leads to increased numerical accuracy, but the computation time is also increased. Therefore, we typically use $65 \times 65 \times 65 = 274,625$ nodes, which for most scenarios lead to results with sufficient numerical accuracy (discussed below). The geometry of the crystal, and the distribution of [U] and [Th] within the crystal, can be specified arbitrarily within this domain.

3.2. Temporal Integration

We use a semi-implicit scheme for the time integration to ensure stability and accuracy. This requires solving a system of equations relating age in the next time step, τ_{new} , to age in the current time step τ_{old} :

$$(D\nabla^2 - 1/(\beta\Delta t))\tau_{new} = \frac{1}{(\beta\Delta t)} [\tau_{old} + \Delta t((1-\beta)D\nabla^2\tau_{old} + P)] \quad (2)$$

where $\beta=0.5 \text{ Ma}^{-1}$ and Δt is the time step duration, set equal to 0.5 Ma here. We use a multigrid method to solve equation (2). Multigrid methods have been used previously in geosciences, in particular in the field of geodynamics [e.g., Tackley, 1993; Tackley and Xie, 2003; Gerya and Yuen, 2007], geophysics [Schinnerl et al., 2000; May and Knepley, 2011], and glacial flow [J. Brown et al., 2013]; see [Brandt, 2002] for a review of multigrid methods. The motivation for the use of multigrid methods is that different wavelengths of the solution to equation (2) can be solved on grids with different resolutions. We use a “V-cycle,” to solve equation (2) using a Gauss-Seidel method to reduce the residual on a series of increasingly coarse grids. The residual is interpolated to a coarser grid and a Gauss-Seidel iteration is performed and this is repeated down to a grid size with $5 \times 5 \times 5$ nodes. We then repeat a similar process by interpolating the residual on to increasingly fine grids and using a Gauss-Seidel iteration on each grid level until the finest grid is reached. Due to this interpolation process from the fine grid to a coarse grid and then back again, this is termed a V-cycle [Brandt, 2002]. Since the diffusivity may evolve as a function of space due to variations in [U] and [Th], we use harmonic averaging to interpolate values of diffusivity from the fine grids to the coarser grids. For each time step, the algorithm is initiated with an initial estimate of the solution, τ_{old} , and we solve equation (2) iteratively until the error is reduced by a factor of 10^7 . Outside of the simulated crystal, τ_{new} is set to zero.

3.3. Validation of Numerical Approach

We compare results obtained using our numerical model to an analytical solution, described in Wolf et al. [1998]. In particular, we simulate the evolution of age, τ , from an initial age of τ^* over time t following heating of the crystal to a fixed temperature:

$$\tau = \frac{a^2}{D} \left[\frac{1}{15} - \sum_{n=1}^{\infty} \frac{6}{\pi^4 n^4} \exp\left(-n^2 \pi^2 \frac{D}{a^2} t\right) \right] + \tau^* \sum_{n=1}^{\infty} \frac{6}{\pi^2 n^2} \exp\left(-n^2 \pi^2 \frac{D}{a^2} t\right) \quad (3)$$

We use a spherical model of radius 100 μm , the activation energy is set to 138 kJ mol^{-1} and the frequency factor is set to 50 $\text{cm}^2 \text{s}^{-1}$ after Farley [2000]. τ^* is set equal to 50 Ma. The analytical solutions for different holding temperatures all show a decrease in age with increased holding time (Figure 3). Initially, the rate at which age decreases is a function of the holding temperature. After some time, a steady state is reached in which the production of ^4He is equal to diffusive loss. The time taken to reach this steady state also depends on the holding temperature, as does the steady state “age.”

For the numerical simulation, we construct a sphere within the domain with a radius of 100 μm . We discretize every dimension into 65 nodes, resulting in grid resolution of approximately 3 μm . For the temporal integration, we use a time step length of 0.5 Ma. The diffusion parameters are identical to those used for the analytical solution. Results show good agreement between the numerical solution and the analytical solution (Figure 5). However, it is important to note that a sphere is poorly approximated with the parameterization employed here. Therefore, the discrepancy between the analytical solution and the numerical solution represents the maximum error that we expect to encounter when using our model.

3.4. Incorporating Crystal-Specific Complexities

The geometry of the crystal and the [U] and [Th] distributions determine where ^4He is produced within the crystal. ^4He that is produced close the edge of the crystal has a predictable rate of being ejected from the crystal due to the effects of the relatively long-stopping distances of alpha-particles [Farley et al., 1996]. Similarly, ^4He that is produced from zones with high [U] and [Th] values is redistributed to regions of low U and Th concentrations due to the long-stopping distance of alpha particles [Ketcham, 2005].

The [U] and [Th] distribution also determines the spatial distribution of diffusivity due to the effects of radiation damage [Shuster et al., 2006; Flowers et al., 2009; Shuster and Farley, 2009]. This effect of spatially variable diffusion kinetics has been incorporated into 1-D spherical approximations, which can be solved

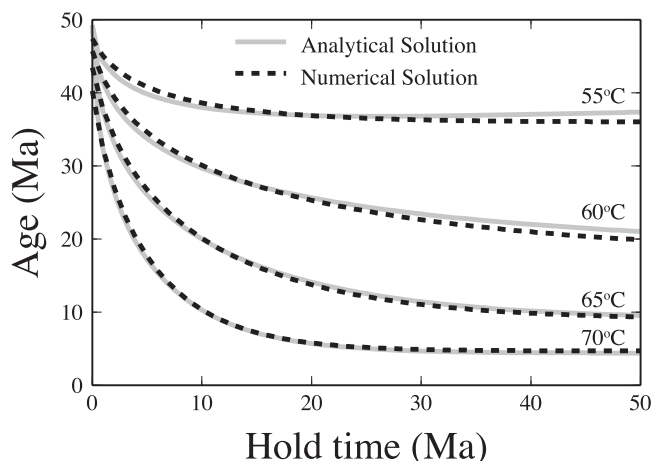


Figure 5. Assessing accuracy of the numerical solution. We simulate the evolution of (U-Th)/He age from an initial value of 50 Ma, following heating to a specific temperature. We use a spherical model of radius 100 μm and diffusion kinetics from Farley [2000]. The numerical solution is shown with the dashed black line and the analytical solution is shown with the solid gray line.

numerically and has proven to be important in applications of $^4\text{He}/^3\text{He}$ thermochronometry [Flowers and Farley, 2012; Fox and Shuster, 2014]. In order to incorporate the measured spatial distribution of [U] and [Th] in 3-D, we must extrapolate the data collected from a two-dimensional section through the crystal across the third dimension. In preparation for LA-ICPMS data collection, crystals are usually mounted such that the polished section is perpendicular to the shortest axis of the crystal. In addition, the crystals are polished so that the measured plane is at the center of the crystal. Therefore, we must estimate a value for the upper and lower surfaces of the crystal, based on the average [U] and [Th] for the edge of the crystal. For the

data presented in Figure 3a, we assume a value of 2 ppm for both the [U] and [Th] values, which is the concentration observed through most of the polished plane (Figure 3a). We then calculate the [U] and [Th] values for other planes perpendicular to the shortest axis by linearly interpolating between the measured section and the estimated concentration at the upper and lower surfaces of the crystal. The number of planes is a function of the grid spacing and the total length of the shortest axis of the crystal. This concept is highlighted in Figure 6. An obvious limitation of this example is that data were collected solely along one polished plane within the crystal. In future applications, our spatial interpolation to 3-D could incorporate LA-ICPMS measurements of several planes either sequentially polished or ablated into the crystal.

We adopt a Monte Carlo procedure to account for complex crystal geometries and [U] and [Th] distributions on the production rate of ^4He [Farley et al., 1996; Hourigan et al., 2005]. We simulate the emission of alpha particles from every node within the crystal using 3000 random vectors. Alpha particles associated with decay of ^{238}U , ^{235}U , and ^{232}Th decay chains have slightly different mean stopping distances (22.83, 19.68, and 22.46 μm , respectively; Farley et al., 1996), and to account for this, the magnitudes of the vectors simulating alpha-particle redistribution from a specific location are a function of the relative abundances of U and Th at that specific location. Comparison of our Monte Carlo simulation with an analytical solution assuming a spherical geometry [Farley et al., 1996] verifies that we produce a sufficient number of random vectors.

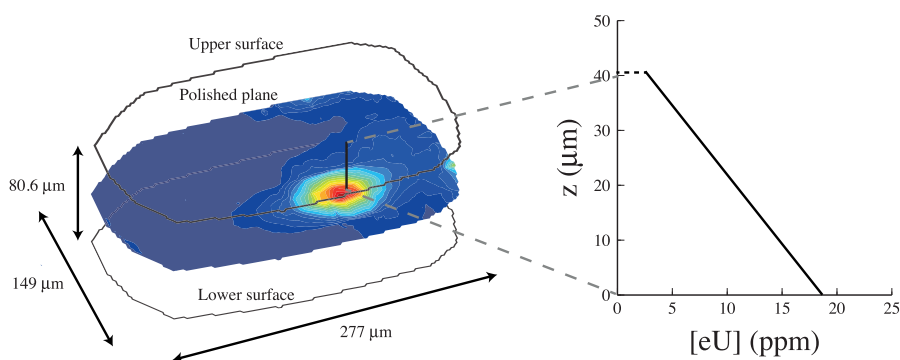


Figure 6. Extrapolation of the 2-D [eU] map in three dimensions. (a) Oblique view of the 2-D [eU] map with same color scale from Figure 1. The dimensions of the crystal were measured using a calibrated optical microscope. We assume that the polished plane is halfway between the upper and lower surfaces of the crystal. (b) Values of [eU] are interpolated from the polished section to the upper surface of the crystal. A [eU] value of 2 ppm is assumed for this upper surface to represent the average [eU] outside of the enriched zone.

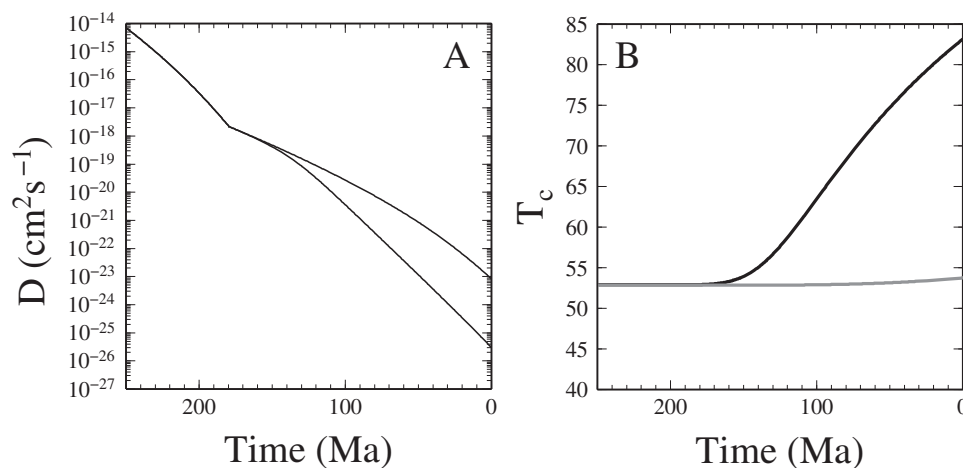


Figure 7. Evolution of diffusivity during cooling. (a) Diffusivity D as a function of the cooling history (Figure 2a). Two curves are shown highlighting two different parts of the crystal with a high [eU] value, black line, and a low [eU] value, gray line. (b) Evolution of apparent closure temperature for a cooling rate of 10/Myr and an effective radius of 100 μm , after Dodson [1973] for the two different locations of the crystal. We stress that we use T_c as a convenient concept to highlight the disparate evolution of radiation damage for different regions of the crystal, not in the interpretation of the thermochronometric age of the crystal.

We also account for the effects of spatial variations in He diffusivity. We use the radiation damage and annealing model, RDAAM [Flowers *et al.*, 2009] to model diffusivity as a function of time at each node within the model. As each node may have different [U] and [Th] values, each may have a different diffusivity, D in equation (1), at a specific temperature. Therefore, we independently model the evolution of diffusivity for each node within the crystal.

4. Results and Discussion

We simulate $^4\text{He}/^3\text{He}$ spectra for the cooling path shown in Figure 4a and the 3-D crystal described above. First, we describe the evolution of diffusivity through time. We then discuss results of the synthetic degassing experiment and implications for spatial variability in radiation damage accumulation.

Using the RDAAM [Flowers *et al.*, 2009] to calculate evolution in ^4He diffusivity, we highlight the divergence in diffusivity for the specified cooling history (Figure 4a) at two control locations within the crystal: (1) within the enriched zone of the crystal where [U] = 21.3 ppm and [Th] = 4.9 ppm; (2) outside of the enriched zone where [U] = 2 ppm and [Th] = 1.9 ppm. In Figure 7a, we show the evolution of D for these two sites within the crystal. The first-order signal is the rapid decrease in diffusivity with decreased temperature. However, due to effects of radiation damage accumulation, ^4He diffusivity within the enriched core decreases more rapidly than for the surrounding portion of the crystal. By 0 Ma (the present day), the predicted difference in diffusivity between the two crystal sites is greater than two orders of magnitude.

A convenient metric to interpret diffusion kinetics is the concept of a closure temperature (T_c ; Dodson, 1973). This is the temperature at the time equivalent to the thermochronometric age of a crystal, assuming a constant cooling rate and for prescribed diffusion kinetics. For illustration, we use a cooling rate of $10^\circ\text{C}/\text{Myr}$ and an effective radius of 100 μm to calculate T_c in Figure 7b. We stress that this conversion is not a physical description of a property of the crystal, rather simply a way to convert diffusion parameters to a more tangible quantity. It is important to note that over the last 150 Ma, the apparent closure temperatures have become separated by almost 30°C due to the effects of radiation damage accumulation (Figure 5b).

Figure 4b shows the model predicted degassing spectra for the time-temperature path of McKeon *et al.* [2014] (shown in Figure 4a) and using our 3-D model of the crystal. The predicted (U-Th)/He age for the crystal is 63.4 Ma; this is within the range of 47.6–185.0 Ma from others crystals dated for this sample [McKeon *et al.*, 2014] and expected based on the relatively low bulk concentration of eU (calculated bulk eU for the modeled crystal is 3.4 ppm). The predicted $^4\text{He}/^3\text{He}$ spectrum is in close agreement with the observed $^4\text{He}/^3\text{He}$ data and the overall patterns are very similar with a concave up spectrum and sharply increasing ratios for $\sum F^3\text{He} > 0.7$. Our analysis is based on several different components, measured, or

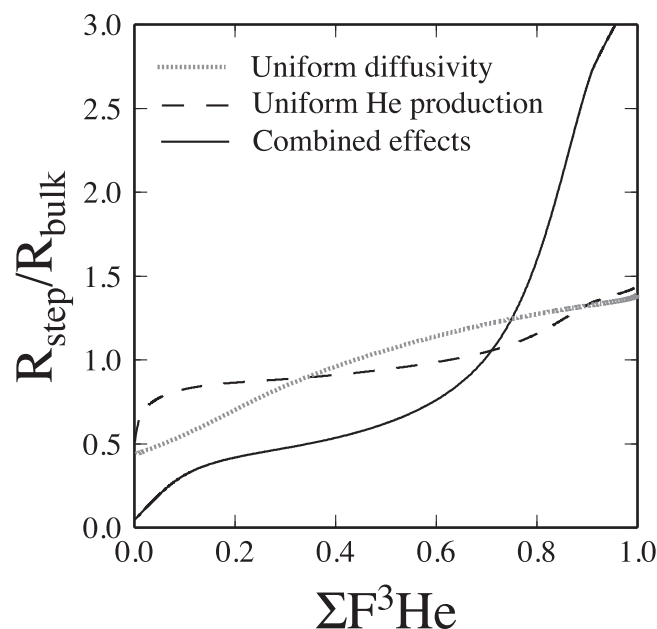


Figure 8. Results of solving the ^4He production-diffusion equation with a 3-D crystal geometry and the prescribed time-temperature path inferred from the analysis of (U-Th)/He age dispersion [McKeon *et al.*, 2014] for three different scenarios. The dotted gray curve shows a model $^4\text{He}/^3\text{He}$ spectrum assuming that He diffusion kinetics is spatially uniform, but ^4He production is a function of the distributions of [U] and [Th]. The dashed black curve shows the same results assuming that diffusion kinetics depends on the spatial distributions of [U] and [Th], but that the ^4He production rate is spatially uniform. The solid black curve highlights the combined effects of spatial variation in diffusivity and ^4He production as in Figure 2b.

low-temperature thermochronologic data from the region [Naeser *et al.*, 2004] and illustrates that at least some portion of the Appalachian landscape has experienced relatively steady and slow evolution. It is beyond the scope of these results to address the spatial variability of cooling histories for different positions in the modern landscape. Furthermore, the simple thermal history used for this example of the 3-D modeling approach does not perfectly fit the observed $^4\text{He}/^3\text{He}$ data, thus there may be more nuance that can be elucidated by modifying the cooling path input to the 3-D model.

The differences between $^4\text{He}/^3\text{He}$ spectra predicted for the zoned models and the spherical crystal approximation with uniform [eU] distribution arise from two main factors. First, low ^4He concentrations outside of the enriched core due to low local production rates cause low $^4\text{He}/^3\text{He}$ ratios for this portion of the crystal with respect to the bulk $^4\text{He}/^3\text{He}$ ratio. Second, this same portion of the crystal experiences a lower radiation dose over the same time interval. In turn, the transition from open to closed system behavior of ^4He occurs at a lower temperature than within the enriched core. Thus ^4He effectively accumulates for a shorter duration in this portion of the crystal and will therefore have a lower $^4\text{He}/^3\text{He}$ with respect to the bulk $^4\text{He}/^3\text{He}$ ratio.

We can isolate the effects of these two contributing factors with two numerical experiments using the same specified time-temperature path shown in Figure 4a. In the first experiment, we assume that the diffusivity of the crystal is spatially uniform but evolves through time as a function of the bulk [eU] value of the crystal. The production of ^4He is a function of the measured [eU] distribution (extrapolated in 3-D) and redistributed by the stopping distances of alpha particles. Results of this experiment are shown in Figure 8 as a dotted gray curve. In contrast, for the second experiment, we assume that the ^4He production rate is spatially uniform, but that diffusivity evolves as a function of space and time based on the measured [eU] distribution (extrapolated in 3-D) and the RDAAM. Results of this experiment are shown in Figure 8 as a dashed black curve. These experiments highlight that only the combined effect of spatial variability in both ^4He production and radiation damage accumulation produce results that are consistent with the data.

The experiments shown in Figure 8 also highlight why the spherically symmetric zoned model (Figure 2b) fails to reproduce the $^4\text{He}/^3\text{He}$ data. The approach used to transform the LA-ICPMS data to radial positions

inferred through a range of novel techniques, which are challenging to validate. These include the ability to map the spatial distribution of uranium and thorium [Farley *et al.*, 2011], accurate measurement of the crystal geometry, RDAAM control on diffusion parameters [Flowers *et al.*, 2009], and a relatively simple thermal model [McKeon *et al.*, 2014]. That the results of the numerical model agree well with the $^4\text{He}/^3\text{He}$ data provides support for each one of these components.

From a geomorphic perspective, the general agreement between the predicted and observed $^4\text{He}/^3\text{He}$ data confirms the time-temperature path reported by McKeon *et al.*, [2014] and it suggests slow and steady exhumation. This sample is from a ridge top at an elevation of $\sim 2,000$ m and is representative of other high ridgelines in the southern Appalachians. The thermal history derived from bulk (U-Th)/He data, and corroborated by $^4\text{He}/^3\text{He}$ data presented here, suggests an erosion rate of ~ 20 m/Ma sustained for the last 180 Ma. This fits with other

leads to spatial averaging of [eU] (Figure 1c). This smears the zone of high [eU] across much of the crystal, leading to less pronounced spatial differences in the evolution of diffusivity and almost uniform distribution of ^4He production. If the [eU] pattern was captured more readily by the radially symmetric model (as would be the case if the zone of high [eU] were to lie at the center of the crystal), then the results obtained using a 3-D model and a spherically symmetric model will be more consistent.

Intercrystal (U-Th)/He age dispersion between crystals from a single rock sample as a function of radiation damage accumulation has been used extensively to quantify, and validate, models of radiation damage control on ^4He diffusion kinetics [Flowers, 2009; Ault *et al.*, 2009; Flowers and Kelley, 2011]. Furthermore, observed age-[eU] relationships have been used to constrain complex geologic thermal histories [Ault *et al.*, 2009; Flowers and Kelley, 2011] since crystals with different bulk [eU] concentrations have different sensitivities to temperatures. Similarly, the additional complexities associated with intracrystal differences in [eU] increases the resolving power of $^4\text{He}/^3\text{He}$ data by introducing additional leverage on constraining the geologic thermal conditions a single sample may have experienced.

Building a 3-D model crystal from a polished 2-D section requires extrapolating information across the third dimension. We have chosen to exploit characteristics of zonation patterns observed from the 2-D section to build a model for the 3-D crystal. In reality, maps of [U] and [Th] at other depths within the crystal could be quite different. As our model-predicted $^4\text{He}/^3\text{He}$ spectrum agrees well with the observed data (Figure 4b), we conclude that our 3-D model of the crystal increases accuracy of the diffusion model in this case. In the future, we plan to ablate the crystal to different depths, which will effectively generate 2-D eU zonation maps at specific depth increments. Such constraints should improve the accuracy of our 3-D [eU] model and eliminate a significant source of uncertainty from the analysis.

5. Conclusions

We have presented a numerical model capable of efficiently solving the ^4He production diffusion equation in three dimensions. This model accounts for the presence of nonsymmetric [U] and [Th] zonation within apatite crystals for interpreting $^4\text{He}/^3\text{He}$ data. [U] and [Th] zonation in apatite, and the resulting disparate accumulation of radiation damage, can lead to zones within a crystal with very different temperature sensitivities. In turn, the intracrystal age dispersion that is detectable using $^4\text{He}/^3\text{He}$ data coupled with LA-ICPMS analysis of the same crystal presents a method to increase the resolving power of $^4\text{He}/^3\text{He}$ thermochronometry. By exploiting parent nuclide zonation observed in an individual crystal in 3-D, we help confirm the radiation damage control of diffusivity observed in crystals with different eU concentrations.

We have shown that a $^4\text{He}/^3\text{He}$ release spectrum from a single apatite crystal from the Appalachian Mountains is consistent with a geologic thermal path constrained by a large population of apatite (U-Th)/He data from the region [McKeon *et al.*, 2014], provided the extreme variations in [eU] within the crystal are incorporated into a 3-D model. However, there are details of the $^4\text{He}/^3\text{He}$ release spectrum that are poorly reproduced by our results, which suggests that modifications to the cooling path may be required. Combined analyses of multiple crystals using this technique could further constrain erosion rates during the Neogene at high elevations across the Appalachian Mountains.

Acknowledgments

We thank P. Tackley for introducing M.F. to the multigrid approach and for sharing part of the code and A. Tripathy-Lang for comments on an early version of this manuscript. This work has been supported by the Swiss National Science Foundation (P2EZP2_148793), the U.S. National Science Foundation grant EAR-1049988 (to D.L.S.), and the Ann and Gordon Getty Foundation. In addition, R.E.M. acknowledges support from several Palmer Research grants from the Earth and Environmental Sciences Department of Lehigh University and to K. Farley at Caltech for help with [U] and [Th] LA-ICPMS analyses.

References

- Ault, A. K., and R. M. Flowers (2012), Is apatite U–Th zonation information necessary for accurate interpretation of apatite (U–Th)/He thermochronometry data?, *Geochim. Cosmochim. Acta*, 79, 60–78.
- Ault, A. K., R. M. Flowers, and S. A. Bowring (2009), Phanerozoic burial and unroofing history of the Western Slave Craton and Wopmay Orogen from apatite (U–Th)/He thermochronometry, *Earth Planet. Sci. Lett.*, 284(1), 1–11.
- Blackmer, G. C., G. I. Omar, and D. P. Gold (1994), Post-Alleghanian unroofing history of the Appalachian Basin, Pennsylvania, from apatite fission track analysis and thermal models, *Tectonics*, 13(5), 1259–1276.
- Boettcher, S. S., and K. L. Milliken (1994), Mesozoic–Cenozoic unroofing of the Southern Appalachian Basin: Apatite fission track evidence from Middle Pennsylvanian sandstones, *J. Geol.*, 102(6), 655–668.
- Brandt, A. (2002), Multiscale scientific computation: Review 2001, in *Multiscale and Multiresolution Methods, Lecture Notes in Computational Science and Engineering*, vol. 20, edited by T. J. Barth, T. Chan, and R. Haimes, pp. 3–95, Springer, Berlin, doi:10.1007/978-3-642-56205-1_1.
- Brown, R. W., R. Beucher, S. Roper, C. Persano, F. Stuart, and P. Fitzgerald (2013), Natural age dispersion arising from the analysis of broken crystals. Part I: Theoretical basis and implications for the apatite (U–Th)/He thermochronometer, *Geochim. Cosmochim. Acta*, 122, 478–497.

- Brown, J., B. Smith, and A. Ahmadi (2013), Achieving textbook multigrid efficiency for hydrostatic ice sheet flow, *SIAM J. Sci. Comput.*, *35*(2), B359–B375.
- Dodson, M. H. (1973), Closure temperature in cooling geochronological and petrological systems, *Contrib. Mineral. Petrol.*, *40*, 259–274.
- Ehlers, T. A., and K. A. Farley (2003), Apatite (U-Th)/He thermochronometry: Methods and applications to problems in tectonic and surface processes, *Earth Planet. Sci. Lett.*, *206*, 1–2.
- Farley, K. A. (2000), Helium diffusion from apatite: General behavior as illustrated by Durango fluorapatite, *J. Geophys. Res.*, *105*(B2), 2903–2914.
- Farley, K. A., R. A. Wolf, and L. T. Silver (1996), The effects of long alpha-stopping distances on (U-Th)/He ages, *Geochim. Cosmochim. Acta*, *60*, 4223–4229, doi:10.1016/S0016-7037(96)00193-7.
- Farley, K. A., D. L. Shuster, E. B. Watson, K. H. Wanser, and G. Balco (2010), Numerical investigations of apatite 4He/3He thermochronometry, *Geochim. Geophys. Geosyst.*, *11*, Q10001, doi:10.1029/2010GC003243.
- Farley, K. A., D. L. Shuster, and R. A. Ketcham (2011), U and Th zonation in apatite observed by laser ablation ICPMS, and implications for the (U-Th)/He system, *Geochim. Cosmochim. Acta*, *75*(16), 4515–4530.
- Fechtig, H., and S. Kalbitzer (1966), The diffusion of argon in potassium-bearing solids, in *Potassium Argon Dating*, edited by A. Schaeffer and J. Zähringer, pp. 68–107, Springer, Berlin, doi:10.1007/978-3-642-87895-4_4.
- Flowers, R., and K. Farley (2012), Apatite 4He/3He and (U-Th)/He evidence for an ancient Grand Canyon, *Science*, *338*(6114), 1616–1619.
- Flowers, R. M. (2009), Exploiting radiation damage control on apatite (U-Th)/He dates in cratonic regions, *Earth Planet. Sci. Lett.*, *277*(1), 148–155.
- Flowers, R. M., and S. A. Kelley (2011), Interpreting data dispersion and ‘inverted’ dates in apatite (U-Th)/He and fission-track datasets: An example from the US midcontinent, *Geochim. Cosmochim. Acta*, *75*(18), 5169–5186.
- Flowers, R. M., R. A. Ketcham, D. L. Shuster, and K. A. Farley (2009), Apatite (U-Th)/He thermochronometry using a radiation damage accumulation and annealing model, *Geochim. Cosmochim. Acta*, *73*(8), 2347–2365.
- Fox, M., and D. L. Shuster (2014), The influence of burial heating on the (U-Th)/He system in apatite: Grand Canyon case study, *Earth Planet. Sci. Lett.*, *397*(0), 174–183, doi:10.1016/j.epsl.2014.04.041.
- Gallen, S. F., K. W. Wegmann, and D. Bohnenstiehl (2013), Miocene rejuvenation of topographic relief in the Southern Appalachians, *GSA Today*, *23*(2), 4–10.
- Gautheron, C., and L. Tassan-Got (2010), A Monte Carlo approach to diffusion applied to noble gas/helium thermochronology, *Chem. Geol.*, *273*(3), 212–224.
- Gautheron, C., L. Tassan-Got, J. Barbarand, and M. Pagel (2009), Effect of alpha-damage annealing on apatite (U-Th)/He thermochronology, *Chem. Geol.*, *266*(3), 157–170.
- Gerya, T. V., and D. A. Yuen (2007), Robust characteristics method for modelling multiphase visco-elasto-plastic thermo-mechanical problems, *Phys. Earth Planet. Inter.*, *163*(1), 83–105.
- Hancock, G., and M. Kirwan (2007), Summit erosion rates deduced from 10Be: Implications for relief production in the Central Appalachians, *Geology*, *35*(1), 89–92.
- Herman, F., J. Braun, T. J. Senden, and W. J. Dunlap (2007), (U-Th)/He thermochronometry: Mapping 3D geometry using micro-X-ray tomography and solving the associated production–diffusion equation, *Chem. Geol.*, *242*(1), 126–136.
- Hourigan, J. K., P. W. Reiners, and M. T. Brandon (2005), U-Th zonation-dependent alpha-ejection in (U-Th)/He chronometry, *Geochim. Cosmochim. Acta*, *69*(13), 3349–3365.
- Huber, C., W. S. Cassata, and P. R. Renne (2011), A lattice Boltzmann model for noble gas diffusion in solids: The importance of domain shape and diffusive anisotropy and implications for thermochronometry, *Geochim. Cosmochim. Acta*, *75*(8), 2170–2186.
- Ketcham, R. A. (2005), Forward and inverse modeling of low-temperature thermochronometry data, *Rev. Mineral. Geochem.*, *58*(1), 275–314.
- Matmon, A., P. Bierman, J. Larsen, S. Southworth, M. Pavich, and M. Caffee (2003), Temporally and spatially uniform rates of erosion in the Southern Appalachian Great Smoky Mountains, *Geology*, *31*(2), 155–158.
- May, D. A., and M. G. Knepley (2011), Optimal, scalable forward models for computing gravity anomalies, *Geophys. J. Int.*, *187*(1), 161–177.
- McDougall, I., and T. M. Harrison (1988), *Geochronology and Thermochronology by the Ar/Ar Method*, Oxford Univ. Press, N. Y.
- McKeon, R. E., P. K. Zeitler, F. J. Pazzaglia, B. D. Idleman, and E. Enkelmann (2014), Decay of an old Orogen: Inferences about Appalachian landscape evolution from low-temperature thermochronology, *Geol. Soc. Am. Bull.*, *126*(1–2), 31–46.
- Meesters, A., and T. Dunai (2002a), Solving the production–diffusion equation for finite diffusion domains of various shapes: Part I. Implications for low-temperature (U-Th)/He thermochronology, *Chem. Geol.*, *186*(3), 333–344.
- Meesters, A., and T. Dunai (2002b), Solving the production–diffusion equation for finite diffusion domains of various shapes: Part II. Application to cases with α -ejection and nonhomogeneous distribution of the source, *Chem. Geol.*, *186*(3), 347–363.
- Miller, D. S., and I. Duddy (1989), Early Cretaceous uplift and erosion of the Northern Appalachian Basin, New York, based on apatite fission track analysis, *Earth Planet. Sci. Lett.*, *93*(1), 35–49.
- Miller, S. R., P. B. Sak, E. Kirby, and P. R. Bierman (2013), Neogene rejuvenation of Central Appalachian topography: Evidence for differential rock uplift from stream profiles and erosion rates, *Earth Planet. Sci. Lett.*, *369*, 1–12.
- Moucha, R., A. M. Forte, J. X. Mitrovica, D. B. Rowley, S. Quéré, N. A. Simmons, and S. P. Grand (2008), Dynamic topography and long-term sea-level variations: There is no such thing as a stable continental platform, *Earth Planet. Sci. Lett.*, *271*(1), 101–108.
- Naeser, N. D., C. W. Naeser, C. S. Southworth, B. Morgan, and A. P. Schultz (2004), Paleozoic to recent tectonic and denudation history of rocks in the Blue Ridge Province, Central and Southern Appalachians—evidence from fission-track thermochronology, *Geol. Soc. Am. Abstr. Programs*, *36*, 114.
- Pavich, M., L. Brown, J. N. Valette-Silver, J. Klein, and R. Middleton (1985), 10Be analysis of a quaternary weathering profile in the Virginia Piedmont, *Geology*, *13*(1), 39–41.
- Pazzaglia, F. J., and M. T. Brandon (1996), Macrogeomorphic evolution of the post-Triassic Appalachian Mountains determined by deconvolution of the offshore basin sedimentary record, *Basin Res.*, *8*(3), 255–278.
- Portenga, E. W., P. R. Bierman, D. M. Rizzo, and D. H. Rood (2013), Low rates of bedrock outcrop erosion in the Central Appalachian Mountains inferred from in situ 10Be, *Geol. Soc. Am. Bull.*, *125*(1–2), 201–215.
- Prince, P. S., and J. A. Spotila (2013), Evidence of transient topographic disequilibrium in a landward passive margin river system: Knickpoints and paleo-landscapes of the new river basin, Southern Appalachians, *Earth Surf. Processes Landforms*, *38*(14), 1685–1699.
- Prince, P. S., J. A. Spotila, and W. S. Henika (2011), Stream capture as driver of transient landscape evolution in a tectonically quiescent setting, *Geology*, *39*(9), 823–826.
- Roden, M. K., and D. S. Miller (1989), Apatite fission-track thermochronology of the Pennsylvania Appalachian Basin, *Geomorphology*, *2*(1), 39–51.

- Schinnerl, M., J. Schoberl, and M. Kaltenbacher (2000), Nested multigrid methods for the fast numerical computation of 3D magnetic fields, *IEEE Trans. Magn.*, *36*(4), 1557–1560.
- Shepard, D. (1968), A two-dimensional interpolation function for irregularly-spaced data, in *Proceedings of the 1968 23rd ACM National Conference, ACM '68*, edited by B.B. Richard, Sr. and M. R. Arthur, pp. 517–524, ACM, N. Y., doi:10.1145/800186.810616.
- Shuster, D. L., and K. A. Farley (2004), $^4\text{He}/^3\text{He}$ Thermochronometry, *Earth Planet. Sci. Lett.*, *217*(1), 1–17.
- Shuster, D. L., and K. A. Farley (2009), The influence of artificial radiation damage and thermal annealing on helium diffusion kinetics in apatite, *Geochim. Cosmochim. Acta*, *73*(1), 183–196.
- Shuster, D. L., K. A. Farley, J. M. Sisterson, and D. S. Burnett (2004), Quantifying the diffusion kinetics and spatial distributions of radiogenic ^4He in minerals containing proton-induced ^3He , *Earth Planet. Sci. Lett.*, *217*(1), 19–32.
- Shuster, D. L., R. M. Flowers, and K. A. Farley (2006), The influence of natural radiation damage on helium diffusion kinetics in apatite, *Earth Planet. Sci. Lett.*, *249*(3), 148–161.
- Shuster, D. L., K. M. Cuffey, J. W. Sanders, and G. Balco (2011), Thermochronometry reveals headward propagation of erosion in an alpine landscape, *Science*, *332*(6025), 84–88.
- Spiegel, C., B. Kohn, D. Belton, Z. Berner, and A. Gleadow (2009), Apatite (U–Th–Sm)/He thermochronology of rapidly cooled samples: The effect of He implantation, *Earth Planet. Sci. Lett.*, *285*(1), 105–114.
- Tackley, P. J. (1993), Effects of strongly temperature-dependent viscosity on time-dependent, three-dimensional models of mantle convection, *Geophys. Res. Lett.*, *20*(20), 2187–2190.
- Tackley, P., and S. Xie (2003), Stag3D: A code for modeling thermo-chemical multiphase convection in Earth's mantle, in *Computational Fluid and Solid Mechanics*, edited by K. J. Bathe, pp. 1524–1527, Elsevier Sci., Oxford, U. K., doi:10.1016/B978-008044046-0.50372-9.
- Tucker, G. E., and Slingerland, R. L., (1994), Erosional dynamics, flexural isostasy, and long-lived escarpments: A numerical modeling study, *J. Geophys. Res.*, *99*(B6), 12,229–12,243.
- Ward, D. J., J. A. Spotila, G. S. Hancock, and J. M. Galbraith (2005), New constraints on the late Cenozoic incision history of the New River, Virginia, *Geomorphology*, *72*(1), 54–72.
- Watson, E. B., K. H. Wanser, and K. A. Farley (2010), Anisotropic diffusion in a finite cylinder, with geochemical applications, *Geochim. Cosmochim. Acta*, *74*(2), 614–633.
- Wolf, R., K. Farley, and D. Kass (1998), Modeling of the temperature sensitivity of the apatite (U–Th)/He thermochronometer, *Chem. Geol.*, *148*(1), 105–114.
- Zeitler, P., A. Herczeg, I. McDougall, and M. Honda (1987), U–Th–He dating of apatite: A potential thermochronometer, *Geochim. Cosmochim. Acta*, *51*(10), 2865–2868.